

Elevated heterotrophic activity in Guaymas Basin hydrothermal plumes influences deep-sea carbon cycling

Received: 9 February 2024

Accepted: 5 May 2025

Published online: 28 May 2025

 Check for updates

Andrew Montgomery¹, Guang-Chao Zhuang^{1,6}, Zhichao Zhou², Marguerite V. Langwig^{2,3}, María del Carmen Millán-Motolinía⁴, Hannah Y. L. Choi¹, Kimberley S. Hunter¹, Carlos A. Mortera-Gutiérrez⁴, Christelle Hyancinthe¹, Zachary Marinelli¹, Karthik Anantharaman², Andreas Teske⁵ & Samantha B. Joye¹✉

Deep-sea hydrothermal plumes are characterized by chemoautotrophic production fueled by the oxidation of reduced inorganic substrates. Recently, organic carbon cycling was proposed, but the metabolic fate of organic carbon is unconstrained. Here, we investigate organic carbon metabolisms in and around a hydrothermal plume to constrain the impacts of hydrothermal vents on deep-sea carbon cycling. Acetate and methanol are detected throughout the water column and are rapidly metabolized in Guaymas Basin waters. Heterotrophic production, up to $7.69 \mu\text{g C L}^{-1} \text{d}^{-1}$, greatly exceeds chemoautotrophic production. Relative to shallow water, elevated microbial activity coincides with a distinct plume signature, indicating that microbial communities respond quickly to hydrothermal inputs. Metatranscriptomic analysis of functional genes for heterotrophic metabolisms implicates Gammaproteobacteria and diverse heterotrophs in hydrothermally-sourced organic carbon degradation. Our results illustrate that organic carbon is differentially cycled within hydrothermal plumes, suggesting that hydrothermal inputs profoundly impact heterotrophic activity in the deep sea.

Hydrothermal discharge occurs along divergent plate boundaries across the global ocean. Superheated, deeply sourced fluids flow through geologic strata, driving geochemical reactions and generating site- or regionally-specific chemical signatures of hydrothermal fluids. These hot fluids mix with overlying seawater upon discharge, creating a dynamic chemical environment that fuels vibrant microbial communities^{1–3}. Hydrothermal plumes are propelled upward and outward in the overlying water column as they move toward natural buoyancy, and the chemicals sourced from plumes can potentially affect seawater composition on a global scale⁴. Because of their

outsized impact on the deep sea, studying hydrothermal plumes can improve our understanding of global biogeochemical cycles.

Chemoautotrophic metabolism is a hallmark of hydrothermal systems; fixation of inorganic carbon coupled to the oxidation of reduced energy-rich substrates forms the base of the food web, driving the proliferation of free-living microbial communities⁵ and microbe-animal symbioses^{6,7}. Many metatranscriptomic-based studies have demonstrated active cycling of sulfur, carbon, hydrogen, and trace metals by the metabolically versatile microbial community in hydrothermal plumes^{4,8–13}. These energy-yielding oxidation reactions

¹Department of Marine Sciences, University of Georgia, Athens, GA, USA. ²Department of Bacteriology, University of Wisconsin-Madison, Madison, WI, USA.

³Freshwater and Marine Sciences Program, University of Wisconsin-Madison, Madison, WI, USA. ⁴Instituto de Geofísica, Universidad Nacional Autónoma de México, C.U. Coyoacán, Ciudad de México, México. ⁵Department of Earth, Marine and Environmental Science, University of North Carolina at Chapel Hill, Chapel Hill, NC, USA. ⁶Present address: Frontiers Science Center for Deep Ocean Multispheres and Earth System (FDOMES) and Key Laboratory of Marine

Chemistry Theory and Technology, Ministry of Education, Ocean University of China, Qingdao, China. ✉ e-mail: mjoye@uga.edu

support dark chemoautotrophic carbon fixation in hydrothermal plumes^{14–16} at rates that rival light-driven carbon fixation rates in the surface ocean¹⁷. Hydrothermal plumes are known to be deep-sea hotspots for chemoautotrophic production.

Heterotrophic metabolisms have received much less attention in hydrothermal plumes. Given the abundance of organic carbon that has been detected^{18,19}, and the diversity of the microbial communities in these plumes, heterotrophic organic matter cycling is likely significant. Previous studies demonstrated that heterotrophic bacteria (e.g., Alpha-, Delta-, and Gammaproteobacteria) are transcriptionally active in plumes^{20–22}, and that carbohydrates are hydrolyzed enzymatically²³. For example, Gammaproteobacteria in hydrothermal plumes actively expressed genes associated with the metabolism of organic sulfur, C-1 compounds, and hydrocarbons¹³. A recent model suggested heterotrophic production in plumes could support fixation of 0.05 GtC y⁻¹ of biomass carbon and thus be a significant contributor to deep-sea carbon cycling²⁴. However, direct measurements of plume organic matter degradation have not been performed, and the contributions of heterotrophs to plume carbon cycling remain unconstrained.

The Guaymas Basin in the Gulf of California is an end-member hydrothermal system where magmatic sill intrusions propagate heat through thick layers of overlying diatomaceous, organic-rich sediments, creating unique and intense fluid discharges²⁵. Discharging hydrothermal fluids are enriched with methane and higher alkanes, low-molecular weight organic carbon compounds, and complex hydrocarbons, including petroleum, that could support diverse heterotrophic microbial metabolisms^{19,26–31}. Metatranscriptomic data from a Guaymas Basin plume showed high transcriptional activity of diverse taxa, including Thioglobaceae, Nitrososphaerota, and SAR324⁹. High oxidation rates of inorganic substrates, such as ammonia and manganese (II), occur in Guaymas Basin hydrothermal plumes, illustrating the importance of chemoautotrophy^{32,33}. Recent studies have also revealed the microbes mediating organic matter cycling in these hydrothermal plumes through meta-omics approaches^{12,13,20,22,34}. However, to fully understand the impact of hydrothermal plumes on carbon cycling, genomics data must be merged with data describing in situ chemistry and microbial activity.

Contemporaneous assessment of metabolic activity and -omics characterizations in hydrothermal plumes are rare, thus limiting our

understanding of ocean biogeochemistry in general. Since chemoautotrophic and heterotrophic processes can occur simultaneously, assessing both suites of processes could offer a new perspective on the microbial ecology of deep-sea hydrothermal plumes. Documenting how microbial communities respond to the rapidly changing chemical regimes in hydrothermal plumes could illuminate the effects of hydrothermally derived energy sources on deep-sea microbial ecology.

We used an interdisciplinary approach to investigate the influence of hydrothermal discharge on carbon cycling in a Guaymas Basin hydrothermal plume. Here, we present direct measurements of organic carbon cycling in a hydrothermal plume, demonstrating a wide range of heterotrophic potential in these systems. We sampled the water column above a hydrothermally active area and captured the signature of a rising hydrothermal plume. To obtain a functional understanding of the hydrothermal plume, we described the chemical regime, constrained microbial activity using radiotracer techniques, and merged those data with functional gene abundance data. Methanol and acetate were considered primary organic substrates for heterotrophic production, and we also measured rates of bicarbonate, naphthalene, hexadecane, and methylamine metabolisms. The results show that organic carbon was rapidly oxidized and assimilated in plumes, underscoring the importance of heterotrophic metabolisms in hydrothermally impacted waters and their contribution to deep-sea carbon cycling.

Results & Discussion

Hydrothermal plume signature

We generated biogeochemical profiles directly in and above a hydrothermal plume and at an adjacent non-plume site near Cathedral Hill²⁵ in the Guaymas Basin (Fig. 1A and B, water depth ~2000 m). Temperature profiles were nearly identical at both sites, ranging from 22 °C near the surface to <4 °C below 1000 m (Fig. 1C and Fig S1). Deviations in temperature and beam transmission during CTD rosette deployment were used to confirm the presence of a hydrothermal plume in real-time. The in-plume site was characterized by temperature anomalies, up to 0.5 °C, and turbidity spikes more than 200 m above the seafloor (Fig. 1C). No temperature or turbidity anomalies were observed at the non-plume site (Fig. S1). During HOV Alvin Dive 5000, the hydrothermal fluids discharging from the vent orifice were

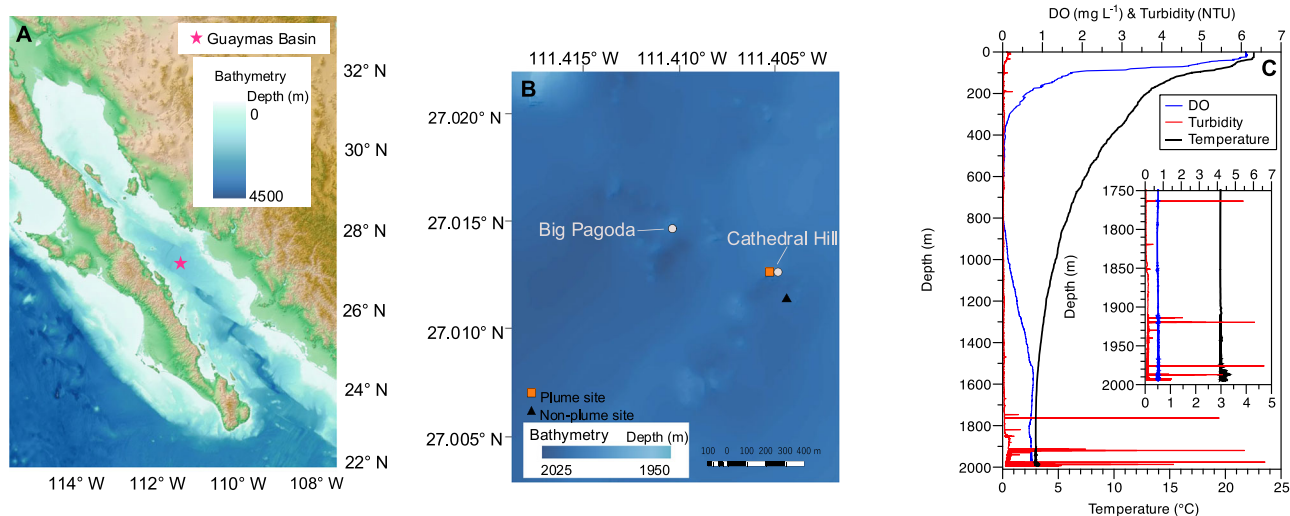


Fig. 1 | Guaymas Basin site maps and CTD profile of the in-plume site. Regional map of the Gulf of California (A) denoting Guaymas Basin, local bathymetry map (B) of each site sampled, and hydrographic profile (C) from the in-plume site at Cathedral Hill. The regional map shows the Gulf of California and Eastern Tropical North Pacific. For (B) the plume and non-plume sites are marked where samples were

collected and the Cathedral Hill and Big Pagoda sites from Teske et al., 2016 are labeled for reference. The Big Pagoda site where the multibeam sonar data depicted in Figure S2 is from, is located approximately 300 m west of the primary Cathedral Hill site. The inset on the CTD plot shows the deepest 250 m of the cast with adjusted axes for clarity. The CTD source data are provided as a Source Data File.

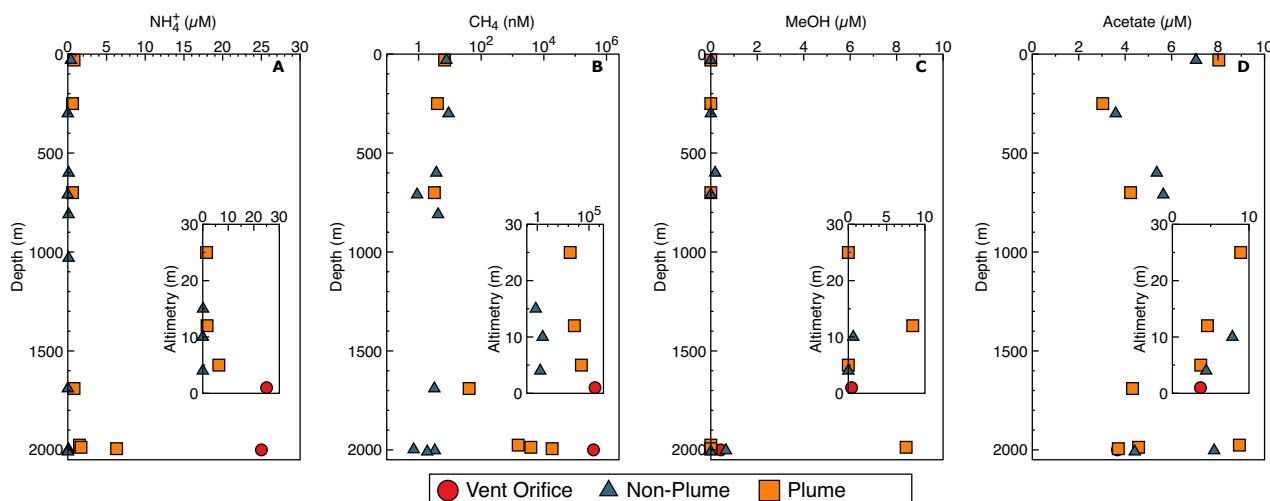


Fig. 2 | Water column chemistry. Depth profiles of ammonium (A), methane (B), methanol (C), and acetate (D) concentrations from the in-plume cast, non-plume cast, and vent orifice sample from AT42-05. Insets are altimetry profiles of the deepest 30 m. Source data are provided as a Source Data file.

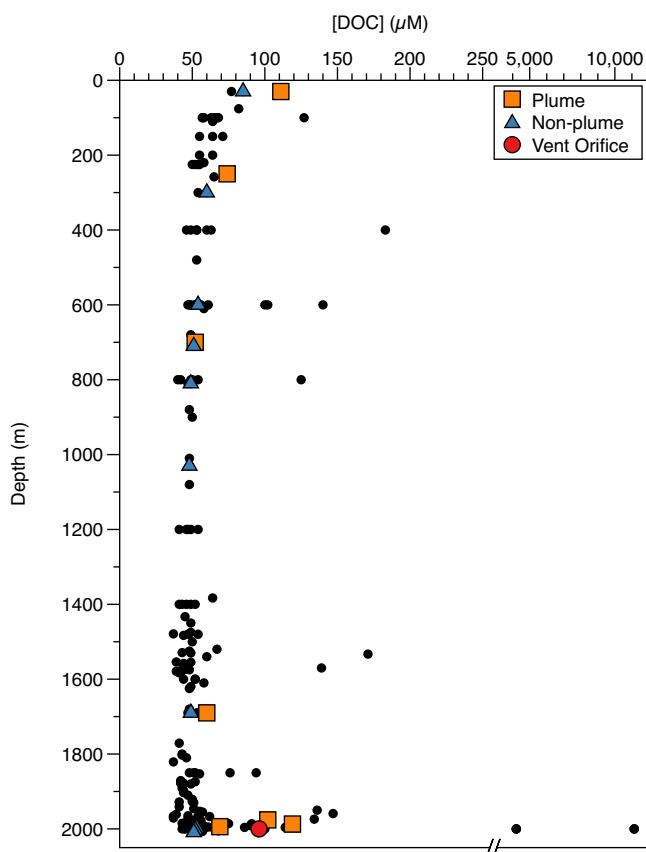


Fig. 3 | Depth profiles of DOC concentrations from three research expeditions (2016–2019) at different sites in the Guaymas Basin. Samples were collected from Niskin bottles on the CTD rosette or attached to the submersible. Colored points were paired with the samples discussed here and the black points represent data from other casts on expedition AT42-05 and two other expeditions. Source data are provided as a Source Data file.

shimmering, which can reflect temperatures above 300 °C³⁵. The temperature of the seawater several meters above the hydrothermal edifice, measured with the HOV Alvin onboard CTD, was -40 °C, illustrating the mixing of hydrothermal fluids with bottom water.

Chemical signatures in the water column further supported the presence of a hydrothermal impact at the in-plume site compared to the non-plume site. Ammonium concentrations ranged from below detection to 25 µM at the vent orifice and were mildly elevated, from 0.6 to 6.3 µM in the plume (Fig. 2A and Supplementary Data 1). In contrast, ammonium concentrations did not exceed 0.4 µM in the non-plume cast. At the in-plume site, dissolved organic carbon (DOC) concentrations ranged from 69–119 µM in the deepest 25 m of the water column, while concentrations were less than 55 µM in the same depth range at the non-plume site (Fig. 3). Across three research expeditions spanning four years (2016–2019), Guaymas Basin DOC concentrations ranged from 40 µM to 11,140 µM in deep-water samples and the highest concentrations were observed in samples collected with the HOV Alvin directly at a vent orifice (Fig. 3). From the in-plume cast, the highest DOC concentration (119 µM) occurred in conjunction with a temperature and turbidity spike -12 m above the seafloor (Figs. 1C and 3). Ammonium and DOC concentrations were significantly higher in the plume than in the non-plume cast (Supplementary Data 8; p -value < 0.05), suggesting a hydrothermal origin of these constituents. Hydrothermally-altered organic matter in Guaymas Basin sediments discharged in the plume could support diverse heterotrophic metabolisms in the overlying water column.

The observed differences in methane concentrations between the two sites were even more drastic. At the vent orifice, the methane concentration was 384 µM, amongst the highest methane concentrations reported for marine waters, and five orders of magnitude higher than the methane concentration in the deepest waters at the non-plume site (Fig. 2B). Elevated methane concentrations persisted up through the water column to a depth of 1690 m (310 m above the seafloor) and were significantly higher (p -value < 0.05; by at least a factor of 10) than any of the non-plume methane concentrations in a comparable depth range (Fig. 2B and Supplementary Data 8). The highest methane concentrations were observed in the deepest samples and concentrations decreased steadily upwards away from the plume source as the hydrothermal fluids were diluted until typical background values (<10 nM) were reached (~1300 m above the seafloor; Fig. 2B). Since methane is a dominant constituent of Guaymas Basin hydrothermal fluids, elevated concentrations in the water column capture the plume signature^{32,36}.

As heated hydrothermal fluids rise through the water column, turbulent mixing entrains the surrounding seawater and dilutes the hydrothermal signature. This mixing disperses reduced compounds

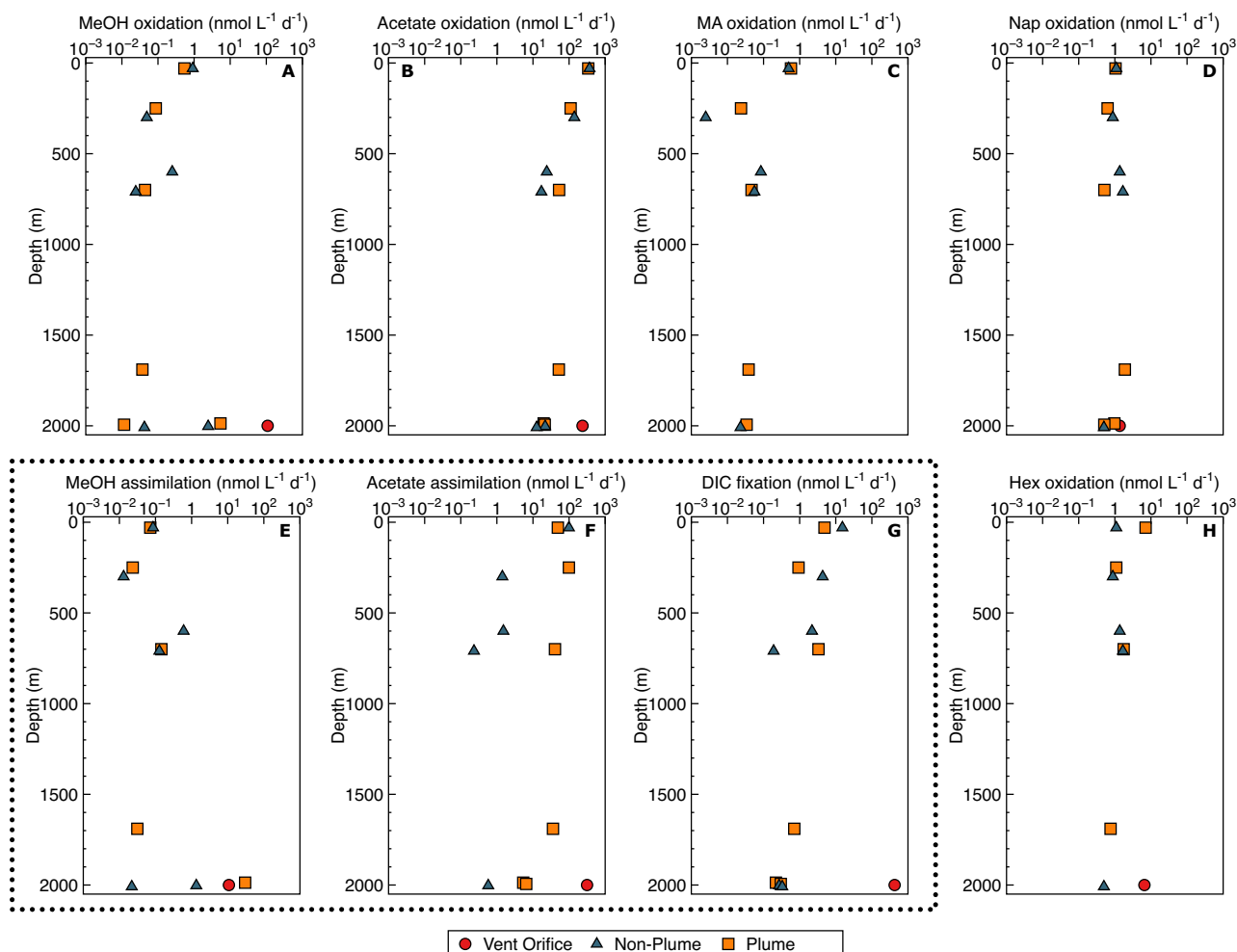


Fig. 4 | Water column metabolic rates. Depth profiles of methanol (MeOH; **A**), acetate (**B**), methylamine (MA; **C**), naphthalene (Nap; **D**) and hexadecane (Hex; **H**) oxidation, methanol (**E**) and acetate (**F**) assimilation and dark carbon fixation (DIC; **G**) rates in the water column of the Guaymas Basin from AT42-05. Assimilatory rates are denoted in the dashed lines. When in situ substrate concentrations were below detection (methanol; 200 nM) or not measured (methylamine, naphthalene, and

hexadecane) the tracer concentration was used for rate calculations. In those cases, potential rates are reported. Methylamine, naphthalene, and hexadecane rates are discussed in the Supplementary Information. Error bars represent standard error of the mean from three live replicates. The values for each rate and the associated turnover constant are provided as a Source Data file.

that can fuel microbial metabolisms³⁷. A computational fluid dynamics model indicated that scalar concentrations of chemical species in the plume can be diluted to less than 10% of the source fluid composition almost immediately after exiting the vent³⁸. However, even with dilution, the acoustic signature of plumes is detectable more than 1600 meters above the seafloor using a multibeam echosounder (Fig. S2), even if the thermal and chemical signatures have dissipated. It is difficult to confirm whether the in-plume samples represent the core of the plume or somewhat diluted peripheral fluids adjacent to the more concentrated core. However, temperature and turbidity anomalies, in conjunction with significantly elevated DOC, methane, and ammonium concentrations, indicate that we successfully targeted the Cathedral Hill hydrothermal plume.

Intense heating in Guaymas Basin sediments and, to some degree, subsequent microbially-mediated cycling of sedimentary organic matter, supply the overlying waters with labile organic carbon, such as acetate, oligosaccharides, hydrocarbons like methane, and other reduced substrates^{19,35}. These energy-rich compounds can fuel a broad array of chemoautotrophic and potentially heterotrophic metabolisms in the deep sea. Therefore, we sought to constrain the extent and magnitude of organic carbon cycling within hydrothermal plumes.

Dynamics of methanol and acetate in the Guaymas Basin water column

We report measurements of methanol concentrations in hydrothermally impacted waters, which ranged from below detection to 8.4 μM (Fig. 2C). Most methanol measurements were below detection (0.2 μM), and there was no significant difference between sites. Methanol concentrations increased from 0.43 μM at the vent orifice to 8.4 μM - 12 m above the seafloor at the in-plume site; this is the highest methanol concentration reported for marine waters.

Acetate concentrations ranged from 3 to 8.9 μM and were relatively uniform throughout the water column (Fig. 2D). Shallower waters were slightly enriched relative to deeper waters, and the highest concentration was observed 25 m above the seafloor at the in-plume site. Subtle differences between the two casts in shallower waters could reflect organic carbon cycling in surface waters and/or the mesopelagic anoxic zone (Fig. 1C). Acetate and methanol are produced during organic matter degradation in Guaymas Basin sediments^{28,31}, and the discharge of hydrothermal fluids enriches the deep sea with these substrates. Hydrothermal fluids are quickly diluted upon discharge into the water column and observed differences in acetate and methanol concentrations likely reflect temporal variability in source

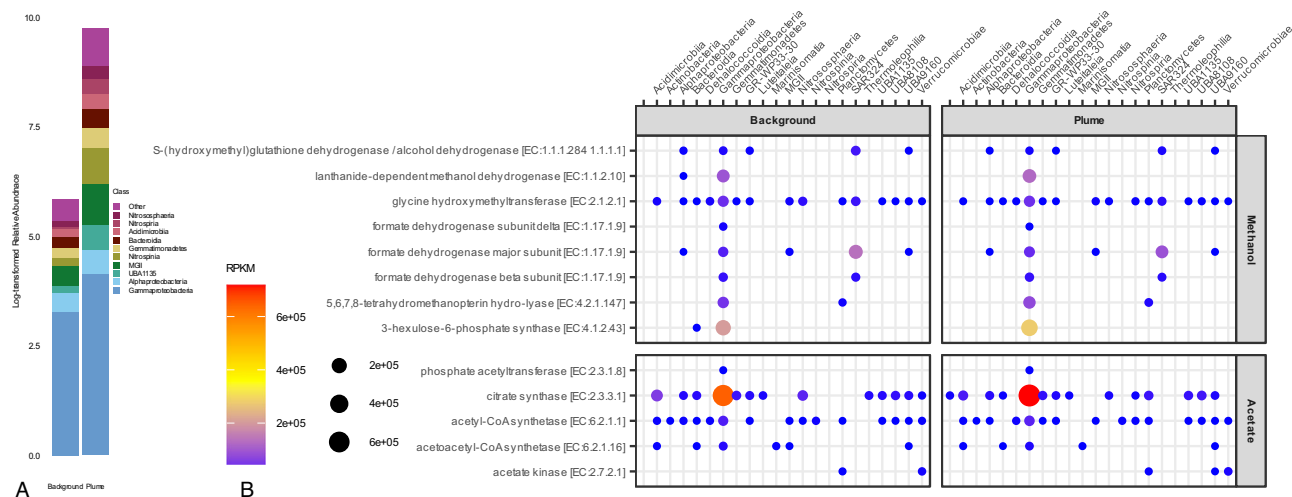


Fig. 5 | Relative abundances of transcripts in the Guaymas Basin water column. **A** Relative abundances of microbial taxa based on mapping of metatranscriptomic data to metagenome-assembled genomes. The ten most abundant classes are shown, and the remaining are grouped in “Other”. Relative abundances were log-transformed. **B** Transcript abundance data of functional genes associated with

acetate and methanol metabolisms and the taxa that harbor them. The abundances of other carbon cycling genes are depicted in Supplementary Fig. 3. RPKM = reads mapped per kilobase of genome per million mapped reads. A link to the source data is provided in the Data Availability section.

fluid composition, physical mixing, or rapid organic matter degradation upon initial discharge.

In the Guaymas Basin water column, the metabolism of all carbon substrates measured was rapid, underscoring that labile organic carbon can act as a carbon and energy source for plume microbial communities (Fig. 4). Methanol and acetate metabolism was observed throughout the water column in both casts and generally, the vent orifice sample, where hydrothermal fluids were minimally diluted, supported the highest rates (and rate constants) for both substrates (Fig. 4A, B–E, F). Turnover constants for methanol oxidation ranged from 0.0013 to 0.092 d⁻¹ and 0.0006 to 0.25 d⁻¹ at the non-plume and in-plume sites, respectively (Supplementary Data 3). The maximum turnover constant was observed at the vent orifice and corresponded to a rate of 108 nmol L⁻¹ d⁻¹ (Fig. 4A and Supplementary Data 2) based on the in situ methanol concentration (0.43 μM, Fig. 2C). These values are comparable to values previously reported for methanol turnover in the Atlantic Ocean and the Gulf of Mexico^{39–41}.

Metagenomic and metatranscriptomic analysis of functional genes from additional plume sites and a background site revealed diverse taxa capable of metabolizing methanol in the Guaymas Basin (Fig. 5A). Metatranscriptomic data indicated that genes encoding methanol dehydrogenase (e.g., *coxF*), the enzyme that oxidizes methanol to formaldehyde⁴², was transcribed by three Gammaproteobacteria lineages (*Methylococcales*, *Betaproteobacteriales*, and UBA4486) in the water column (Fig. 5B). Members of the *Methylococcales* order are methanotrophs and leverage methanol dehydrogenase for aerobic methane oxidation. Elevated transcriptional activity of *coxF* by *Methylococcales* (Fig. 5B) points to the importance of aerobic methanotrophy in Guaymas Basin hydrothermal plumes. In contrast, members of the *Betaproteobacteriales* belonging to the *Methylophilaceae* family are obligate methylotrophs that assimilate methanol via the ribulose monophosphate pathway⁴³. Transcripts associated with this pathway (e.g., 3-hexulose-6-phosphate synthase) were highly transcribed in the plume and mapped to *Methylophilaceae*, indicating this group plays a role in methanol metabolism. Much less is known about the UBA4486 group, but a recent study suggested they are facultative methylotrophs⁴⁴. The transcriptional activity of *coxF* associated with UBA4486 was higher than the *Methylophilaceae*, suggesting UBA4486 may contribute significantly to methanol cycling in Guaymas Basin plumes.

Acetate oxidation turnover constants fell within a comparable range to methanol oxidation, ranging from 0.0028 to 0.052 d⁻¹ and 0.00042 to 0.064 d⁻¹ at the non-plume and in-plume sites, respectively (Supplementary Data 3). These turnover constants corresponded to oxidation rates ranging from 12.6 to 367.4 nmol L⁻¹ d⁻¹ (Fig. 4B and Supplementary Data 2). Maximum rates were observed in surface waters, but acetate oxidation was also high at the vent orifice (235.8 ± 60.8 nmol L⁻¹ d⁻¹). The injection of acetate produced in the subsurface primes the plume for elevated oxidation rates. Additionally, the strong correlation between acetate oxidation and temperature (Fig. 6) and the highest turnover constant being observed near the vent orifice (Supplementary Data 3, in situ temperature ~40 °C) indicated that temperature and, by extension, hydrothermal fluid input is an essential factor regulating acetate metabolism in the Guaymas Basin water column.

Acetate metabolism is initiated by the production of acetyl-CoA either by ligation of acetate and coenzyme A or catalyzed by the acetyl-CoA synthetase enzyme. This process is associated with the acetate kinase-phosphate acetyltransferase pathway⁴⁵ and the citric acid cycle⁴⁶. The genes encoding these enzymes were actively transcribed in the Guaymas Basin water column and implicated the role diverse heterotrophic bacteria in acetate metabolism (Fig. 5B and Fig. S3). The acetyl-CoA synthetase gene (encoded by *acs*) was transcribed by 17 unique classes in the Guaymas Basin water column, and most transcripts were associated with the Gammaproteobacteria (Fig. 5). Similarly, transcription of the citrate synthase gene was widespread and was the most transcribed gene by the Gammaproteobacteria (Fig. 5B). This group was also implicated in amino acid and carbohydrate metabolism (Fig. S3). Members of the Gammaproteobacteria are metabolically versatile, emphasizing the role this group plays in organic carbon cycling in the Guaymas Basin and other hydrothermal vent ecosystems⁴⁷.

The availability of energy-rich organic substrates in the water column supports a diverse microbial population engaged in multiple metabolic pathways that drive dynamic carbon cycling in the water column. This environment promotes sustained microbial activity across taxa, as is reflected in the consistent transcriptional levels observed between the in-plume and non-plume sites (Fig. 5B and Fig. S3). This pervasive response indicates a basal level of metabolic readiness within the water column that allows the microbial

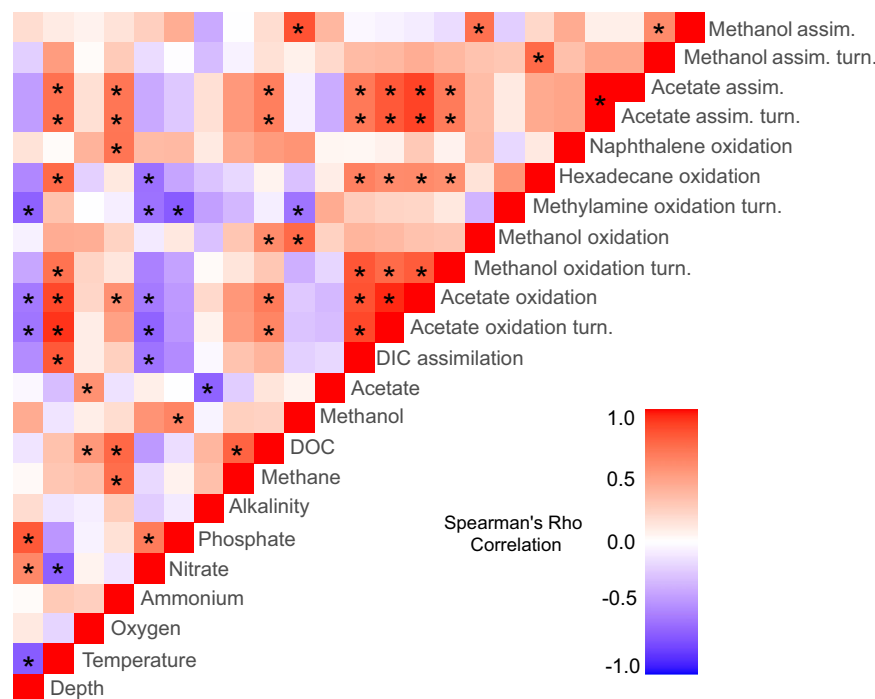


Fig. 6 | Spearman's Rho rank correlation coefficients of relationships between biogeochemical parameters and rate measurements. Stars represent relationships that were statistically significant (p -value < 0.05). Turnover refers to turnover constants. Raw data and correlation statistics are provided as a Source Data file.

community to respond quickly to changes in substrate availability. The Gammaproteobacteria exemplify this adaptability since they exhibit rapid growth rates when responding to environmental perturbations, including increased availability of organic matter or internal recycling of carbon^{48,49}. These capabilities drive the high relative abundance of the Gammaproteobacteria (Fig. 5) and support their dominant role in acetate and methanol metabolism, and drive elevated heterotrophy within the Guaymas Basin water column.

Heterotrophic production from methanol and acetate

Heterotrophic methanol and acetate assimilation into biomass were also detected in Guaymas Basin waters. Assimilatory turnover constants ranged from below detection to 0.25 d^{-1} for methanol, while acetate assimilation ranged up to 0.09 and 0.014 d^{-1} at the in-plume and non-plume sites, respectively (Supplementary Data 5). Maximum turnover constants for both substrates were observed near the vent orifice where hydrothermal inputs are minimally diluted, and DOC concentrations were elevated (Fig. 3). The maximum methanol assimilation rate ($30.4 \pm 5.7 \text{ nmol L}^{-1} \text{ d}^{-1}$) was observed 12 m above the seafloor where the highest methanol concentration was observed (Fig. 4E and Supplementary Data 4).

Acetate assimilation was significantly higher at the in-plume site (Supplementary Data 8) and was positively correlated with temperature, and DOC and ammonium concentrations (Fig. 6). Acetate assimilation was highest at the vent orifice ($314.6 \pm 11.4 \text{ nmol L}^{-1} \text{ d}^{-1}$) and was below detection in the deepest sample at the non-plume site. Acetate supplied by the venting fluids could support this difference. However, warmer temperatures and other hydrothermal constituents from the venting fluids may have indirectly stimulated acetate metabolism at the vent orifice, especially since acetate was uniformly present throughout the water column (Fig. 3D).

While methanol and acetate were readily oxidized for energy conservation, heterotrophic uptake of these substrates was often comparable to or higher than oxidation rates. For example, acetate

assimilation accounted for 59% of the total uptake (sum of oxidation and assimilation) at the vent orifice, while methanol assimilation accounted for 85% of total uptake 12 m above the seafloor (Table 1). Elevated assimilation and oxidation of these substrates are maintained by temperature anomalies near the vent and the injection of hydrothermally derived DOC (Fig. 3) into the deep sea. Additionally, ammonium supplied from the vent (Fig. 2A) could support elevated methanol assimilation (and oxidation). Ammonium addition supported higher rates of methanol assimilation in the Gulf of Mexico⁴¹. Our results indicated that microbial populations inhabiting the deep waters near Guaymas Basin hydrothermal vents can quickly respond to organic carbon inputs for energy conservation and biomass production.

The discharge of hydrothermal fluids from vents directly connects the subsurface with plumes and overlying water column, delivering elevated concentrations of DOC¹⁹ and other biologically relevant elements to deep waters across the basin (Fig. 3 and Supplementary Data 1). This discharge influences biogeochemical cycling and shapes the deep-sea microbial community⁵⁰. The microbial population that responds to these inputs and ultimately becomes entrained in the plume originates from the water column rather than the seafloor⁹, meaning they respond to hydrothermal inputs after discharge from the vent. The microbial response time must be rapid because the rising velocity of hydrothermal fluids is fast, causing immediate and continuous dilution of the hydrothermal signature⁵¹. Residence times in the rising plume may be less than 1 hour³⁷. However, our data contrast with previous models, which suggest microbial activity in the plume is insignificant^{37,38}. Instead, we demonstrate that the deep-sea microbial community responds quickly to organic carbon input from hydrothermal sources. This response drives the high rates of activity observed near the vent orifice and contributes to the biogeochemical signature of the entire basin. Taken together, this suggests the microbial community near the vent orifice responds rapidly to the input of organics, which contributes to the high rates of heterotrophy observed in this study.

Table 1 | Relative contributions of oxidation and assimilation to acetate and methanol uptake

Site	Depth (m)	Altimetry (m)	Acetate uptake (d ⁻¹)	Fraction oxidation (%)	Fraction assimilation (%)	Methanol uptake (d ⁻¹)	Fraction oxidation (%)	Fraction assimilation (%)
NP	30	1982.79	0.0661	78.77	21.23	0.1002	91.46	8.54
NP	300	1712.79	0.0384	98.97	1.03	0.0062	78.95	21.05
NP	600	1412.79	0.0039	92.71	7.29	0.0043	29.18	70.82
NP	710	1302.79	0.0022	98.11	1.89	0.0152	15.91	84.09
NP	810	1202.79	N.D.	N.D.	N.D.	N.D.	N.D.	N.D.
NP	1030	982.79	N.D.	N.D.	N.D.	N.D.	N.D.	N.D.
NP	1690	322.79	N.D.	N.D.	N.D.	N.D.	N.D.	N.D.
NP	1998	14.79	N.D.	N.D.	N.D.	N.D.	N.D.	N.D.
NP	2003	9.79	0.0020	96.23	3.77	0.0058	64.62	35.38
NP	2009	3.79	0.0023	100.00	0.00	0.0064	65.62	34.38
IP	30	1968.59	0.0479	87.31	12.69	0.0670	88.30	11.70
IP	250	1750.72	0.0714	49.51	50.49	0.0121	78.76	21.24
IP	700	1299.2	0.0222	52.11	47.89	0.0207	23.16	76.84
IP	1690	308.59	N.D.	N.D.	N.D.	N.D.	N.D.	N.D.
IP	1976	24.72	0.0080	44.22	55.78	0.0075	54.12	45.88
IP	1987	12.2	0.0047	72.48	27.52	0.0042	15.03	84.97
IP	1994	4.59	0.0076	74.56	25.44	0.0013	100.00	0.00
VO	2000	1	0.1593	40.28	59.72	0.2745	90.99	9.01

Uptake is the sum of oxidation and assimilation. Percent contributions were calculated as fraction of total uptake (assimilation of oxidation turnover constant/uptake ×100. NP non-plume cast, IP in-plume cast, VO vent orifice sample, N.D. Not determined.

Table 2 | Dark carbon fixation and heterotrophic assimilation rates

Site	Depth (m)	Altimetry (m)	DIC fixation		MeOH assimilation		Acetate assimilation		MeOH + Acetate	
			ng C L ⁻¹ d ⁻¹	SE	ng C L ⁻¹ d ⁻¹	SE	ng C L ⁻¹ d ⁻¹	SE	ng C L ⁻¹ d ⁻¹	SE
NP	30	1982.79	183.22	4.38	1.03	0.10	2378.95	103.33	2379.98	103.41
NP	300	1712.79	52.08	8.07	0.16	0.04	34.09	7.73	34.25	7.72
NP	600	1412.79	26.37	8.02	5.10	1.66	36.41	7.12	41.52	5.52
NP	710	1302.79	2.32	0.79	1.02	0.45	5.58	1.44	4.74	1.36
NP	810	1202.79	N.D.	N.D.	N.D.	N.D.	N.D.	N.D.	N.D.	N.D.
NP	1030	982.79	N.D.	N.D.	N.D.	N.D.	N.D.	N.D.	N.D.	N.D.
NP	1690	322.79	N.D.	N.D.	N.D.	N.D.	N.D.	N.D.	N.D.	N.D.
NP	1998	14.79	N.D.	N.D.	N.D.	N.D.	N.D.	N.D.	N.D.	N.D.
NP	2003	9.79	3.30	0.58	16.16	2.14	13.85	5.31	30.01	6.45
NP	2009	3.79	4.01	1.52	0.18	0.08	0.00	0.00	0.18	0.08
IP	30	1968.59	58.62	7.14	0.86	0.08	1174.60	53.82	1175.46	53.83
IP	250	1750.72	11.12	2.10	0.28	0.03	2373.37	331.00	2373.65	331.02
IP	700	1299.2	39.87	9.32	1.75	0.74	976.80	50.00	978.55	50.46
IP	1690	308.59	N.D.	N.D.	N.D.	N.D.	N.D.	N.D.	N.D.	N.D.
IP	1976	24.72	8.48	1.75	0.26	0.07	860.65	421.64	860.92	421.69
IP	1987	12.2	2.62	1.43	247.14	68.68	129.05	15.82	376.19	64.23
IP	1994	4.59	3.61	1.05	BDL	0.01	156.22	68.27	156.22	68.27
VO	2000	1	5128.44	205.87	129.62	10.20	7556.20	273.89	7685.82	277.16

NP non-plume cast, IP in-plume cast, VO vent orifice sample, N.D. Not determined, B.D.L. below detection limit.

Comparison of inorganic carbon fixation and heterotrophic plume production

To explore the dynamics of heterotrophic and autotrophic metabolisms in the Guaymas Basin we made contemporaneous measurements of dark carbon fixation and heterotrophic carbon assimilation rates. Dark carbon fixation rates ranged from 0.002 to 5.12 μg C L⁻¹ d⁻¹, with the maximum activity observed at the vent orifice (Table 2 and Fig. 4G). Inorganic carbon fixation rates were comparable to rates measured at

the Galápagos rift vents⁵². Highly reduced inorganic substrates are energy sources for chemoautotrophic production in hydrothermal plumes⁵³. We observed ammonium concentrations up to 25 μM (Fig. 2A and Supplementary Data 1) at the in-plume site, which could support ammonia oxidizing Nitrososphaerota (formerly Thaumarchaeota) in Guaymas Basin plumes^{8,32}. Nitrososphaerota efficiently fix bicarbonate via the 3-hydroxypropionate/4-hydroxybutyrate pathway and play a crucial role in marine carbon cycling⁵⁴. However, the abundance of

genes associated with this pathway (E6.2.1.56 and *abfD*; Fig. S4) was relatively low or below detection.

Guaymas Basin plumes are also enriched with methane (Fig. 2B), sulfide, iron, manganese, and hydrogen³⁵ in addition to DOC (e.g., methanol; Fig. 3). These substrates are oxidized by Thioglobaceae, SAR324, and Epsilonproteobacteria^{9,55,56} for energy conservation during chemoautotrophic growth. Since the chemical signature of the plume can influence microbial community composition^{57,58} and transcriptional activity⁹, metabolisms associated with inorganic carbon fixation and heterotrophic production should be important in these plumes. Similarly, genes associated with other autotrophic carbon fixation pathways (e.g. rTCA or Calvin–Benson–Bassham cycles) were sparsely detected in Guaymas Basin plumes (Fig. S4).

Until now, the relative contribution of heterotrophic metabolisms in hydrothermal plumes has not been measured directly. Heterotrophic production from acetate and methanol ranged from below detection up to 7.5 and 0.25 $\mu\text{g C L}^{-1} \text{d}^{-1}$, respectively (Table 2). Throughout the water column, combined heterotrophic production significantly exceeded dark carbon fixation rates (Supplementary Data 8 and 9), often by more than an order of magnitude. Combined heterotrophic production was significantly higher than dark carbon fixation at the plume site (Supplementary Data 9) and the two were indistinguishable at the non-plume site. Heterotrophy commonly exceeds chemoautotrophy in marine waters, which could explain some of the differences in the Guaymas Basin. However, the enrichment of DOC, acetate, and methanol coincided with elevated concentrations of chemoautotrophic substrates in the plume (Fig. 2, 3), where dark carbon fixation would be expected to dominate. The availability of organic substrates supported heterotrophic assimilation rates that were significantly higher (Supplementary Data 9) than dark carbon fixation by a factor of ~143. Microbial oxidation at the vent orifice and abiotic reactions in the cold oxygenated seawater likely decreased the pool of reduced inorganic substrates and may have limited dark carbon fixation at depths above the vent orifice. Additionally, heterotrophic fixation of inorganic carbon could couple the oxidation of organic matter to dark carbon fixation (e.g., at the vent orifice)⁵⁹. In contrast, the relatively larger pool of DOC persisted in the rising plume (Fig. 3) to support heterotrophic metabolisms. This may explain the low relative abundance of functional genes associated with chemoautotrophic metabolisms observed in the rising plume (Fig. S2).

Although acetate and methanol are a substantial fraction of the DOC pool, anabolism of these compounds only provides a partial glimpse into total prokaryotic heterotrophic production. Transcripts of diverse aminotransferases were abundant, and a wide range of CAZymes were detected in the Guaymas Basin water column (Fig. S3), indicating that other organic substrates, such as carbohydrates²³ and amino acids¹⁹, are viable carbon sources for biomass production in hydrothermal plumes. A recent model suggested heterotrophic production rates in hydrothermal plumes could be sustained up to 0.0124 $\mu\text{g C L}^{-1} \text{d}^{-1}$ ²⁴. However, DOC concentrations in Guaymas Basin (Fig. 3) are substantially higher than the values supplied to the model by Cathalot et al. Notably, their work focused on mid-ocean ridges with lower DOC concentrations and did not include Guaymas Basin, which could explain the discrepancies between the model and our rate data. Our data shows that plume microbial communities can support heterotrophic production rates several orders of magnitude higher from just methanol and acetate alone (up to 7.6 $\mu\text{g C L}^{-1} \text{d}^{-1}$). Given the widespread availability of DOC in Guaymas Basin (Fig. 3), total prokaryotic heterotrophic production rates are likely higher than the combined assimilation rates reported here. Our data reveal a rapid heterotrophic response to hydrothermal organic carbon inputs by deep-sea microbial communities at rates comparable to or greater than plume chemoautotrophic production.

The magnitude of plume heterotrophic production will depend on many factors, including the bioavailability of the discharged DOC

pool. Guaymas Basin has a unique hydrothermal signature relative to other hydrothermal systems, making these plumes more conducive to heterotrophic production³⁵. At mid-ocean ridge hydrothermal systems, fluids are enriched with gaseous hydrocarbons⁶⁰, and thermal alteration of complex organic matter can produce more labile forms of carbon at the Mid-Atlantic Ridge⁶¹. Guaymas Basin hydrothermal fluids also contain hydrocarbons, which are metabolized throughout the water column (see Supplementary Information). Similarly, formate and acetate (up to 158 and 35 $\mu\text{mol kg}^{-1}$, respectively) have been detected at the Lost City hydrothermal field¹⁸, which could potentially fuel heterotrophic metabolisms in the ensuing plumes. Metabolism of these substrates near vents could be supported by microbial taxa that inhabit the deep sea. For example, heterotrophic Gammaproteobacteria and Campylobacteria are widespread in hydrothermal ecosystems⁶². Functional redundancy has been documented across hydrothermal systems with distinct geochemistry and microbial populations^{63,64} suggesting heterotrophic production could dominate when other hydrothermal plumes are enriched with organic carbon. Ultimately, more studies that measure heterotrophic production and DOC concentrations in hydrothermal plumes are needed to constrain the extent of organic carbon cycling within plumes.

Historically, dark carbon fixation coupled to oxidation of reduced inorganic compounds has been considered the foundation of biomass production in hydrothermal vent ecosystems. Our results expand on this, illustrating that carbon is differentially and significantly cycled within hydrothermal plumes. Elevated concentrations of methane (up to 380 μM), methanol (up to 8 μM), acetate (up to 8.9 μM), and DOC (up to 1,140 μM) were detected. Hydrothermal vents supply deep-sea microbial communities with energy from these and other energy-rich substrates, as evidenced by the high oxidation rates observed here, underscoring their importance for deep-sea carbon cycling. The organic carbon compounds studied here were generally used as energy sources, however, assimilatory activity accounted for a significant portion of uptake (up to 85%). These data demonstrate the importance of dark carbon fixation in hydrothermal plumes and reveal that heterotrophic production can dominate chemoautotrophic production. Taken together, our data suggest hydrothermal vents profoundly impact local organic carbon cycling within hydrothermal plumes and likely contribute significantly to oceanic biogeochemical cycling.

Methods

Sample collection

We collected seawater samples during R/V Atlantis expedition AT42-05 to Guaymas Basin in November 2018. Samples for chemical analysis, rate measurements, and molecular surveys were collected with 20 L Niskin bottles attached to a rosette (water column profiles) or with 5 L Niskin bottles mounted on the HOV Alvin (vent orifice sample) near the Cathedral Hill site (Fig. 1B; 27°00.696 N, 111°24.265 W)²⁵. During expedition AT42-05, one CTD cast collected fluids directly above a venting edifice at Cathedral Hill (in-plume). The other targeted a site approximately 200 m to the southeast of the primary vent, serving as an off-site comparison (non-plume). Hydrographic profiles were obtained with a Seabird CTD-rosette system to assess the presence of a hydrothermal plume signature. The HOV Alvin sample was collected within 2 m of the vent orifice using a submersible-mounted Niskin bottle.

Upon return to the deck, Niskin bottles were sub-sampled immediately for dissolved methane concentration by filling a He-purged 160 mL serum vial headspace-free⁶⁵. Each serum vial contained 10 g of NaCl and 3 NaOH pellets, was filled with seawater from the corresponding Niskin bottle, and then capped with a blue butyl rubber stopper and sealed with an aluminum crimp seal⁶⁶. Directly after collecting dissolved methane samples, an acid-washed 1 L polyethylene terephthalate glycol (PETG) bottle was filled with water from the same

Niskin bottle for chemical analysis and rate assays and capped headspace free. Bottles were stored at 4 °C until processing. Chemistry samples for subsequent analyses of nutrients, DOC, acetate, and methanol were preserved within 6 hours on board the ship by passing through a 0.2 µm pore-size filter (Target® filter)⁶⁷. Samples were either processed shipboard or frozen at -20 °C for subsequent shore-based analysis, except methanol samples, which were stored at -80 °C⁶⁸.

Chemical measurements

Ammonium samples (5 mL, 0.2 µm filtered) were preserved with phenol and stored at 4 °C until analysis. Ammonium concentrations were measured on the ship within two days of collection using the phenol hypochlorite method; standards were prepared from ACS reagent grade NH₄Cl (Sigma), and the detection limit was 0.1 µM⁶⁹. In the UGA lab, DOC and total dissolved nitrogen (TDN) concentrations were quantified by high-temperature combustion using a Shimadzu Instruments TOC-V TNM⁶⁷. Standards were prepared from potassium hydrogen phthalate and the detection limit was 2 µM. Other chemical parameters such as nitrate, nitrite, and ortho-phosphate were also measured⁶⁷.

Unfiltered samples for methanol quantification were collected in combusted 38 mL serum vials, stoppered with a blue butyl rubber stopper, and crimp sealed. Concentrations were determined using an SRI gas chromatograph equipped with a purge and trap system, an MXT[®]-Q-PLOT column (30 m x 0.52 mm I.D., Restek), and a flame-ionizing detector^{41,68}. Aqueous methanol standards made using analytical grade methanol (Sigma) in a matching chemical matrix; the detection limit was 200 nM. Samples for acetate quantification were passed through an 0.2 µm filter and frozen at -20 °C until further processing. Once thawed, samples were derivatized and analyzed via High Performance Liquid Chromatography (Dionex) equipped with an UV/Vis detector⁷⁰. Aqueous standards were generated from analytical grade acetate (Sigma) in artificial seawater. The detection limit was 1 µM.

To quantify methane concentration, a headspace of 60 mL (in plume and vent orifice samples) or 10 mL (out of plume samples) was created in each serum vial by replacing an equal volume of brined sample with ultra-high purity (UHP) N₂ gas through the stopper with a needle and syringe⁶⁵. Headspace methane was determined by injecting 800 µL of gas into a 200 µL sample loop plumbed to a GC-FID (Shimadzu, model 8610 C) equipped with an Alltech Carbosphere 80/100 column (Part No. C-5000). Final methane concentrations were calculated using aqueous standards of known concentration produced from gaseous methane standards (Airgas)^{65,71}. The detection limit was ~0.75 nM methane.

Multibeam hydroacoustic data processing

We used multibeam surveys to obtain the location and height of a hydrothermal plume in the Guaymas Basin water column. The Multibeam Echosounder System (EM301, 30 kHz, Kongsberg) used for data collection was outfitted onboard the R/V Falkor⁷². Bathymetry data were processed with Qimera software (v2.4.9, QPS) and water column data were processed with FMMidwater (v7.9.4, QPS); both using the EPSG Geodetic Database (v9.9.1) for georeferencing hydroacoustic data, following International Hydrographic Organization guidelines⁷³. The metadata for the files generated from hydrographic surveys are described in Supplementary Data 10.

Data obtained from Marv1.0 software (<https://predmar.cicese.mx/>), a predictive time series referenced to the mean sea level of the corresponding station, were used for tidal correction. A digital elevation model was generated to describe the location and height of the hydrothermal plume. No artifacts from latency errors or lack of lateral splicing were observed, and scattered data were invalidated through software cleaning filters and manual retouching. The resolution ranged from 5 to 10 m, and visualization of acoustic images was generated

from multibeam files 78, 80, 92, 179, and 210 (Supplementary Data 10). Visualizations were processed with Fledermaus software 7.9 (QPS, 2021). Full data resolution was maintained during file import to identify the plume's characteristics in the water column. To improve image quality, we used boundary filtering based on the bathymetric depth of the water column, the vertical range of the echogram, and beam suppression according to angular opening. The plume boundaries were manually selected based on the fan acoustic cone view.

Statistical analysis

Statistical analyses were performed in R (version 3.4.4). Means of methane and methanol concentrations, turnover constants, and rates were compared using the Tukey-Kramer HSD test. Data were log-transformed prior to statistical analyses and *p*-values of <0.05 were considered statistically significant. Correlations between hydrographic data, geochemical data, rate constants, and rate data were assessed non-parametrically using Spearman's rank correlation with the `cor.test()` function in R (version 3.4.4).

Rate measurements

We assessed oxidation and assimilation rates of methanol, acetate, methylamine, bicarbonate, hexadecane, and naphthalene using radiotracer techniques in discrete water samples. Water samples were collected from Niskin bottles as described above and stored at 4 °C until processing. Within 6 hours of sample collection, seawater was transferred to incubation vials using an open-bore 60 mL syringe fitted with silicone tubing to minimize disruption of particle-associated microorganisms⁷¹. Incubation vials were overfilled with three volumes and sealed headspace-free to avoid the exchange of dissolved gases. There were three live replicates and a killed control for each discrete depth. Killed controls were amended with a solution to halt biological activity before radiotracer injection (see below). The temperatures for rate incubations were as near to in situ temperature as possible and always fell within 10% of the temperature reading from the CTD for a given depth. Samples were incubated for one or two days, depending on substrate and depth, to ensure adequate tracer turnover in live samples relative to killed controls. Live incubations were terminated with the amendment of the appropriate kill solution (see below) to preserve them for shore-based analysis. Microbial oxidation and assimilation rates were quantified by tracking the conversion of radiolabeled substrate to ¹⁴CO₂ or ¹⁴C- biomass.

Seawater samples to measure oxidation or assimilation of methanol, methylamine, or acetate were injected with 100 µL of each ¹⁴C-labeled aqueous radiotracer. Final radiotracer activities and substrate concentrations are reported in Supplementary Data 7. Radiotracer incubations were carried out in 38 mL serum vials that were stoppered with a blue butyl rubber stopper, crimp-sealed, and incubated^{41,74}. After incubation (~2 d), a 20 mL subsample to measure assimilation into biomass was removed from the sealed serum vial using a syringe and needle (displaced with lab air) to a clean 50 mL centrifuge tube. Biological activity was terminated immediately by adding 1 mL of 100% trichloroacetic acid (5% final concentration, TCA). The remaining 18 mL sample volume in the sealed vial (for oxidation rates) was amended immediately with 1 mL of 100% TCA to halt biological activity.

Upon transporting the samples back to the UGA lab, we quantitatively measured the oxidation of these three substrates to ¹⁴CO₂^{41,74}. The evolved ¹⁴CO₂ was quantitatively trapped (>90% recovery) in 1.5 mL of 3-methoxypropylamine (MilliporeSigma) in 4.5 mL of scintillation fluid (Biosafe II, Research Products International, Mount Prospect, IL) and counted using a Tricarb 2910TR liquid scintillation analyzer (Perkin Elmer). Radiolabeled methanol, methylamine, or acetate assimilated into biomass was quantified by filtering samples through a 0.2 µm polyethersulfone filter (MilliporeSigma), rinsing three times with 0.5% TCA in 35 ppt NaCl solution (pH ~3) to remove

any residual ^{14}C -bicarbonate or unused substrate, and counting the filter in 6 mL of scintillation fluid.

Dark bicarbonate fixation rates were measured by quantifying the uptake of ^{14}C -bicarbonate into biomass. Seawater was subsampled into a 38 mL serum vial with no headspace and stoppered with gray chlorobutyl septa, crimp sealed, and injected with 100 μL of aqueous ^{14}C -bicarbonate tracer (1×10^6 Bq). Samples were incubated for 48 to 60 hr. Biological activity was terminated with formaldehyde (3.7% v/v final concentration), and samples were processed like the assimilation samples described above.

Hydrocarbon oxidation rates were determined by tracking the production of $^{14}\text{CO}_2$ from labeled naphthalene and hexadecane⁷⁵. Briefly, samples were transferred to 7 mL scintillation vials and sealed headspace-free with PTFE-lined septa to prevent tracer adsorption. Samples were injected with 20 μL of tracer (Supplementary Data 7, dissolved in 200 proof ethanol) using a glass syringe to avoid tracer loss and incubated for ~1 d. Incubations were terminated by transferring samples to 15 mL centrifuge tubes with 1 mL of 2 M NaOH to trap $^{14}\text{CO}_2$ and halt biological activity. Back in the lab, samples were shaken with activated charcoal to irreversibly trap unused tracer and then distilled to quantify the production of $^{14}\text{CO}_2$ by acid digestion (5 mL $\text{H}_3\text{PO}_4 > 85\%$ wt.). Volatilized $^{14}\text{CO}_2$ was quantitatively trapped (>90% recovery) in 7 mL scintillation vials containing $\frac{1}{4}$ of a glass fiber filter and 1.5 mL of 3-methoxypropylamine. After a 6 hr distillation, samples were amended with 4.5 mL of scintillation fluid and counted on the scintillation counter. Process blanks and standards with known radioactivity were measured routinely to assess recovery efficiency.

Rate calculations

Turnover constants, k (d^{-1}), were calculated as the ratio (f) of recovered ^{14}C (i.e., $^{14}\text{CO}_2$ for organic substrate oxidation or ^{14}C -biomass for assimilation) product counts to the activity (disintegrations per minute; DPM) of the substrate initially added divided by incubation time (t):

$$\text{Turnover constant} = k = f/t \quad (1)$$

$$f = \text{DPM} - \text{product} / \text{DPM} - \text{substrate} \quad (2)$$

Substrate turnover time (d) was the inverse of turnover constants ($1/k$). Killed controls were used to correct for background tracer turnover and were typically comparable to instrument background counts. Rates were calculated by multiplying in situ substrate concentration by k :

$$\text{Oxidation or Assimilation Rate} = [\text{substrate}] * k \quad (3)$$

If substrate concentration was not measured (i.e. hydrocarbons and methylamine) potential rates were estimated based on the substrate concentration from tracer amendment. For some of these compounds, tracer-added concentrations may have exceeded the in situ concentration, and thus, those rates may reflect potential activity.

Metagenomic sample collection and sequencing

On a subsequent cruise to Guaymas Basin during expedition FK190211 aboard R/V Falkor in February and March 2019 we collected additional water from several rising plumes for metagenomic analysis. The details of these sampling sites are presented in Supplementary Data 6. Briefly, seawater was collected via CTD rosette as described above and up to 4 L of water was passed through an 0.2 μm Sterivex filter (Millipore-Sigma). Excess liquid was removed from the filters, and they were immediately flash frozen in liquid nitrogen. Subsequently, samples were stored at -80°C for nucleic acid extraction. DNA was extracted from frozen filters using a Qiagen Dneasy PowerSoil Max extraction kit and sent to COSMOS ID for sequencing.

Metagenomic assembly and binning

The raw reads underwent QC followed by processing and trimming by metaWRAP v1.3.2 using default settings⁷⁶. The metagenomic assemblies were obtained by SPAdes v3.12.0 using the following options “-k 21,33,55,77,99,127 -m 900 -t 48 --meta”⁷⁷. All reads of samples, including hydrothermal plume and marine background samples, were assembled individually. The reads from four hydrothermal plume samples from Guaymas Basin sites, including Big Pagoda site 24, 26, 27, and 29 samples, were additionally combined and subjected to co-assembly. Assembly coverages were obtained using Bowtie2 v2.4.5⁷⁸ and CoverM (<https://github.com/wwood/CoverM>) by mapping the corresponding metagenomic reads. The metagenome-assembled genomes (MAGs) were obtained by metaWRAP v1.3.2 using the assemblies and assembly coverages generated in the above steps with default settings.

The resulting MAGs with genome completeness >50% and contamination <10% were further subjected to bin refinement to screen heterogeneous scaffolds potentially originating from contamination and erroneously assigned 16S rRNA sequences using RefineM v0.0.24⁷⁹. In addition, manual checks were conducted using VizBin⁸⁰ to further refine the MAGs by choosing scaffolds that were clustered by coverage and 5-nucleotide k-mer patterns.

Metagenome assembled genome taxonomy and functional annotation

GTDB-Tk v0.1.3⁸¹ with GTDB release R86 was used to assign taxonomy for all MAGs that passed quality filters and refinement. METABOLIC v4.0⁸² was used to annotate MAGs and generate metabolic profiles and functional networks using default settings. The functional gene abundance was parsed from the METABOLIC results and normalized to one million reads per metagenome, facilitating parallel comparison across all samples. MAGs were also annotated with DRAM v1.4.6⁸³, and the subcellular localization of DRAM-derived CAZyme annotations was obtained using PSORTb v3.0⁸⁴.

Metatranscriptome read mapping

We used publicly available Guaymas Basin metatranscriptomes SRR452448 (in-plume) and SRR453184 (non-plume, NCBI, BioProject PRJNA72707) to determine the expression of the Guaymas Basin MAGs and their functional genes. CoverM v0.6.1 (<https://github.com/wwood/CoverM>) was used to calculate the relative abundance of MAGs using the following command line options: coverm genome --coupled --methods relative_abundance. For relative abundance, all 146 MAGs were mapped to the two Guaymas Basin metatranscriptomes. The expression level of functional genes (RPKM) was calculated with CoverM, where 64 functional genes were mapped to the two metatranscriptomes using the following command line options: coverm contig --coupled --methods rpkm. These functional genes include extracellular CAZymes, as well as amino acid and fatty acid degradation genes. CoverM-calculated relative abundance and RPKM values were parsed and visualized in R (Figs. 5, S2, and S3).

Reporting summary

Further information on research design is available in the Nature Portfolio Reporting Summary linked to this article.

Data availability

All chemical and rate data generated for this study are included in the Supplementary Information/Source Data file. These data have also been submitted to the NOAA National Centers for Environmental Information (NCEI) under accession code 0288839 (<https://www.ncei.noaa.gov/archive/archive-management-system/OAS/bin/prd/jquery/accession/details/288839>). Sequencing data are publicly available through NCBI under BioProject code PRJNA72707.

References

- Perner, M. et al. In situ chemistry and microbial community compositions in five deep-sea hydrothermal fluid samples from Irina II in the Logatchev field. *Environ. Microbiol.* **15**, 1551–1560 (2013).
- Reysenbach, A. L. & Shock, E. Merging genomes with geochemistry in hydrothermal ecosystems. *Science* **296**, 1077–1082 (2002).
- Reysenbach, A. L., Banta, A. B., Boone, D. R., Cary, S. C. & Luther, G. W. Microbial essentials at hydrothermal vents. *Nature* **404**, 835 (2000).
- Dick, G. J. et al. The microbiology of deep-sea hydrothermal vent plumes: Ecological and biogeographic linkages to seafloor and water column habitats. *Front. Microbiol.* **4**, 1–16 (2013).
- Sievert, S. M. & Vetriani, C. Chemoautotrophy at deep-sea vents: Past, present, and future. *Oceanography* **25**, 218–233 (2012).
- Dubilier, N., Bergin, C. & Lott, C. Symbiotic diversity in marine animals: The art of harnessing chemosynthesis. *Nat. Rev. Microbiol.* **6**, 725–740 (2008).
- Petersen, J. M. et al. Hydrogen is an energy source for hydrothermal vent symbioses. *Nature* **476**, 176–180 (2011).
- Baker, B. J., Lesniewski, R. A. & Dick, G. J. Genome-enabled transcriptomics reveals archaeal populations that drive nitrification in a deep-sea hydrothermal plume. *ISME J.* **6**, 2269–2279 (2012).
- Lesniewski, R. A., Jain, S., Anantharaman, K., Schloss, P. D. & Dick, G. J. The metatranscriptome of a deep-sea hydrothermal plume is dominated by water column methanotrophs and lithotrophs. *ISME J.* **6**, 2257–2268 (2012).
- Anantharaman, K., Breier, J. A., Sheik, C. S. & Dick, G. J. Evidence for hydrogen oxidation and metabolic plasticity in widespread deep-sea sulfur-oxidizing bacteria. *PNAS* **110**, 330–335 (2013).
- Anantharaman, K. et al. Sulphur oxidation genes in diverse deep-sea viruses. *Science* **344**, 757–760 (2014).
- Li, M., Jain, S., Baker, B. J., Taylor, C. & Dick, G. J. Novel hydrocarbon monooxygenase genes in the metatranscriptome of a natural deep-sea hydrocarbon plume. *Environ. Microbiol.* **16**, 60–71 (2014).
- Zhou, Z. et al. Gammaproteobacteria mediating utilization of methyl-, sulfur- and petroleum organic compounds in deep ocean hydrothermal plumes. *ISME J.* **14**, 3148 (2020).
- Karl, D. M., Wirsén, C. O. & Jannasch, H. W. Deep-sea primary production at the Galápagos hydrothermal vents. *Science* **207**, 1345–1347 (1980).
- Wirsén, C. O., Jannasch, H. W. & Molyneux, S. J. Chemosynthetic microbial activity at Mid-Atlantic Ridge hydrothermal vent sites. *J. Geophys. Res.* **98**, 9693–9703 (1993).
- Amend, J. P., McCollom, T. M., Hentscher, M. & Bach, W. Catabolic and anabolic energy for chemolithoautotrophs in deep-sea hydrothermal systems hosted in different rock types. *GCA* **75**, 5736–5748 (2011).
- Prakash, A., Sheldon, R. W. & Sutcliffe, W. H. Geographic variation of oceanic ^{14}C dark uptake. *Limnol. Oceanogr.* **36**, 30–39 (1991).
- Lang, S. Q., Butterfield, D. A., Schulte, M., Kelley, D. S. & Lilley, M. D. Elevated concentrations of formate, acetate and dissolved organic carbon found at the Lost City hydrothermal field. *GCA* **74**, 941–952 (2010).
- Lin, Y. S. et al. Near-surface heating of young rift sediment causes mass production and discharge of reactive dissolved organic matter. *Sci. Rep.* **7**, 1–10 (2017).
- Li, M. et al. Genomic and transcriptomic evidence for scavenging of diverse organic compounds by widespread deep-sea archaea. *Nat. Commun.* **6**, 8933 (2015).
- Meier, D. V. et al. Heterotrophic Proteobacteria in the vicinity of diffuse hydrothermal venting. *Environ. Microbiol.* **18**, 4348–4368 (2016).
- Wang, W., Li, Z., Zeng, L., Dong, C. & Shao, Z. The oxidation of hydrocarbons by diverse heterotrophic and mixotrophic bacteria that inhabit deep-sea hydrothermal ecosystems. *ISME J.* **14**, 1–13 (2020).
- Ziervogel, K. & Arnosti, C. Substantial carbohydrate hydrolase activities in the water column of the Guaymas Basin (Gulf of California). *Front. Mar. Sci.* **6**, 1–8 (2020).
- Cathalot, C. et al. Hydrothermal plumes as hotspots for deep-ocean heterotrophic microbial biomass production. *Nat. Commun.* **12**, 6861 (2021).
- Teske, A. et al. The Guaymas Basin hiking guide to hydrothermal mounds, chimneys, and microbial mats: Complex seafloor expressions of subsurface hydrothermal circulation. *Front. Microbiol.* **7**, 75 (2016).
- Kawka, O. E. & Simoneit, B. R. T. Survey of hydrothermally-generated petroleum from the Guaymas Basin spreading center. *Org. Geochem.* **11**, 311–328 (1987).
- Welhan, J. A. & Lupton, J. E. Light hydrocarbon gases in Guaymas Basin hydrothermal fluids: thermogenic versus abiogenic origin. *Am. Assoc. Petr. Geol. Bull.* **71**, 215–223 (1987).
- Martens, C. S. Generation of short chain acid anions in hydrothermally altered sediments of the Guaymas Basin, Gulf of California. *Appl. Geochem.* **5**, 71–76 (1990).
- Peter, J. M., Peltonen, P., Scott, S. D., Simoneit, B. R. T. & Kawka, O. E. 14 C ages of hydrothermal petroleum and carbonate in Guaymas Basin, Gulf of California: implications for oil generation, expulsion, and migration. *Geology* **19**, 253–256 (1991).
- Cowen, J. P., Wen, X. & Popp, B. N. Methane in aging hydrothermal plumes. *GCA* **66**, 3563–3571 (2002).
- Zhuang, G. et al. Generation and utilization of volatile fatty acids and alcohols in hydrothermally altered sediments in the Guaymas Basin, Gulf of California. *Geophys. Res. Lett.* **46**, 2637–2646 (2019).
- Lam, P., Cowen, J. P. & Jones, R. D. Autotrophic ammonia oxidation in a deep-sea hydrothermal plume. *FEMS Microbiol. Ecol.* **47**, 191–206 (2004).
- Dick, G. J. et al. Enzymatic microbial Mn(II) oxidation and Mn bio-oxide production in the Guaymas Basin deep-sea hydrothermal plume. *GCA* **73**, 6517–6530 (2009).
- Li, M., Jain, S. & Dick, G. J. Genomic and transcriptomic resolution of organic matter utilization among deep-sea bacteria in Guaymas Basin hydrothermal plumes. *Front. Microbiol.* **7**, 1–13 (2016).
- Von Damm, K. L., Edmond, J. M., Measures, C. I. & Grant, B. Chemistry of submarine hydrothermal solutions at Guaymas Basin, Gulf of California. *GCA* **49**, 2221–2237 (1985).
- Whelan, J. K., Simoneit, B. R. T. & Tarafa, M. E. C1-C8 hydrocarbons in sediments from Guaymas Basin, Gulf of California-comparison to Peru Margin, Japan Trench and California Borderlands. *Org. Geochem.* **12**, 171–194 (1988).
- Reed, D. C. et al. Predicting the response of the deep-ocean microbiome to geochemical perturbations by hydrothermal vents. *ISME J.* **9**, 1857–1869 (2015).
- Jiang, H. & Breier, J. A. Physical controls on mixing and transport within rising submarine hydrothermal plumes: A numerical simulation study. *Deep-Sea Res. I. Pap.* **92**, 41–55 (2014).
- Dixon, J. L., Beale, R. & Nightingale, P. D. Rapid biological oxidation of methanol in the tropical Atlantic: significance as a microbial carbon source. *Biogeosciences* **8**, 2707–2716 (2011).
- Sargeant, S. L., Murrell, J. C., Nightingale, P. D. & Dixon, J. L. Basin-scale variability of microbial methanol uptake in the Atlantic Ocean. *Biogeosciences* **15**, 5155–5167 (2018).
- Zhuang, G., Peña-Montenegro, T. D., Montgomery, A., Hunter, K. S. & Joye, S. B. Microbial metabolism of methanol and methylamine in the Gulf of Mexico: insight into marine carbon and nitrogen cycling. *Environ. Microbiol.* **20**, 4543–4554 (2018).
- Chistoserdova, L. Modularity of methylotrophy, revisited. *Environ. Microbiol.* **13**, 2603–2622 (2011).

43. Doronina, N., Kaparullina, E. & Trotsenko, Y. The Family Methylophilaceae. in *The Prokaryotes: Alphaproteobacteria and Betaproteobacteria* (eds. Rosenberg, E., DeLong, E. F., Lory, S., Stackebrandt, E. & Thompson, F.) 869–880 (Springer, Berlin, Heidelberg, 2014). https://doi.org/10.1007/978-3-642-30197-1_243.
44. Francis, B., Urich, T., Mikolasch, A., Teeling, H. & Amann, R. North Sea spring bloom-associated Gammaproteobacteria fill diverse heterotrophic niches. *Environ. Microbiome* **16**, 15 (2021).
45. Zhang, S. et al. Metabolic engineering for efficient supply of acetyl-CoA from different carbon sources in *Escherichia coli*. *MCF* **18**, 130 (2019).
46. Guzman Barron, E. S. & Ghiretti, F. The pathways of acetate oxidation. *Biochim. Biophys. Acta* **12**, 239–249 (1953).
47. Trembath-Reichert, E., Butterfield, D. A. & Huber, J. A. Active seafloor microbial communities from Mariana back-arc venting fluids share metabolic strategies across different thermal niches and taxa. *ISME J.* **13**, 2264–2279 (2019).
48. Peña-Montenegro, T. D. et al. Species-specific responses of marine bacteria to environmental perturbation. *ISME Commun.* **3**, 99 (2023).
49. Mikan, M. P. et al. Metaproteomics reveal that rapid perturbations in organic matter prioritize functional restructuring over taxonomy in western Arctic Ocean microbiomes. *ISME J.* **14**, 39–52 (2020).
50. Dick, G. J. The microbiomes of deep-sea hydrothermal vents: distributed globally, shaped locally. *Nat. Rev. Microbiol.* **17**, 271–283 (2019).
51. Converse, D. R., Holland, H. D. & Edmond, J. M. Flow rates in the axial hot springs of the East Pacific Rise (21°N): implications for the heat budget and the formation of massive sulfide deposits. *Earth Planet. Sci. Lett.* **69**, 159–175 (1984).
52. Tuttle, J. H., Wirsén, C. O. & Jannasch, H. W. Microbial activities in the emitted hydrothermal waters of the Galápagos rift vents. *Mar. Biol.* **73**, 293–299 (1983).
53. McCollom, T. M. Geochemical constraints on primary productivity in submarine hydrothermal vent plumes. *Deep-Sea Res. I. Pap.* **47**, 85–101 (2000).
54. Könneke, M. et al. Ammonia-oxidizing archaea use the most energy-efficient aerobic pathway for CO₂ fixation. *PNAS* **111**, 8239–8244 (2014).
55. German, C. R. et al. Diverse styles of submarine venting on the ultraslow spreading Mid-Cayman Rise. *PNAS* **107**, 14020–14025 (2010).
56. Sheik, C. S. et al. Spatially resolved sampling reveals dynamic microbial communities in rising hydrothermal plumes across a back-arc basin. *ISME J.* **9**, 1434–1445 (2015).
57. Anantharaman, K., Breier, J. A. & Dick, G. J. Metagenomic resolution of microbial functions in deep-sea hydrothermal plumes across the Eastern Lau Spreading Center. *ISME J.* **10**, 225–239 (2016).
58. Meier, D. V. et al. Niche partitioning of diverse sulfur-oxidizing bacteria at hydrothermal vents. *ISME J.* **11**, 1545–1558 (2017).
59. Braun, A. et al. Reviews and syntheses: Heterotrophic fixation of inorganic carbon – significant but invisible flux in environmental carbon cycling. *Biogeosciences* **18**, 3689–3700 (2021).
60. Baumberger, T. et al. Fluid composition of the sediment-influenced Loki’s Castle vent field at the ultra-slow spreading Arctic Mid-Ocean Ridge. *GCA* **187**, 156–178 (2016).
61. Rossel, P. E. et al. Thermally altered marine dissolved organic matter in hydrothermal fluids. *Org. Geochem.* **110**, 73–86 (2017).
62. Zhou, Z., St. John, E., Anantharaman, K. & Reysenbach, A.-L. Global patterns of diversity and metabolism of microbial communities in deep-sea hydrothermal vent deposits. *Microbiome* **10**, 241 (2022).
63. Galambos, D., Anderson, R. E., Reveillaud, J. & Huber, J. A. Genome-resolved metagenomics and metatranscriptomics reveal niche differentiation in functionally redundant microbial communities at deep-sea hydrothermal vents. *Environ. Microbiol.* **21**, 4395–4410 (2019).
64. Reysenbach, A., St. E., Meneghin, J., Flores, G. E. & Podar, M. Complex subsurface hydrothermal fluid mixing at a submarine arc volcano supports distinct and highly diverse microbial communities. *PNAS* **117**, 32627–32638 (2020).
65. Magen, C. et al. A simple headspace equilibration method for measuring dissolved methane. *Limnol. Oceanogr. Methods* **12**, 637–650 (2014).
66. Joye, S. B., MacDonald, I. R., Leifer, I. & Asper, V. Magnitude and oxidation potential of hydrocarbon gases released from the BP oil well blowout. *Nat. Geosci.* **4**, 160–164 (2011).
67. Joye, S. B. et al. The anaerobic oxidation of methane and sulfate reduction in sediments from Gulf of Mexico cold seeps. *Chem. Geol.* **205**, 219–238 (2004).
68. Zhuang, G.-C., Lin, Y.-S., Elvert, M., Heuer, V. B. & Hinrichs, K.-U. Gas chromatographic analysis of methanol and ethanol in marine sediment pore waters: Validation and implementation of three pretreatment techniques. *Mar. Chem.* **160**, 82–90 (2014).
69. Solórzano, L. Determination of Ammonia in Natural Waters by the Phenylhypochlorite Method. *Limnol. Oceanogr.* **14**, 799–801 (1969).
70. Albert, D. B. & Martens, C. S. Determination of low-molecular-weight organic acid concentrations in seawater and pore-water samples via HPLC. *Mar. Chem.* **56**, 27–37 (1997).
71. Rogener, M. K., Bracco, A., Hunter, K. S., Saxton, M. A. & Joye, S. B. Long-term impact of the Deepwater Horizon oil well blowout on methane oxidation dynamics in the northern Gulf of Mexico. *Elementa* **6**, 1–17 (2018).
72. Urban, P., Köser, K. & Greinert, J. Processing of multibeam water column image data for automated bubble/seep detection and repeated mapping. *Limnol. Oceanogr.: Methods* **15**, 1–21 (2017).
73. International Hydrographic Organization. *IHO Standards for Hydrographic Surveys*, Edition 6.1.0. 42 <https://repository.oceanbestpractices.org/handle/11329/388.3>, <https://doi.org/10.25607/OBP-1354.3> (2022).
74. Zhuang, G., Peña-Montenegro, T. D., Montgomery, A., Montoya, J. P. & Joye, S. B. Significance of Acetate as a Microbial Carbon and Energy Source in the Water Column of Gulf of Mexico: Implications for Marine Carbon Cycling. *Glob. Biogeochem. Cycles* **33**, 223–235 (2019).
75. Kleindienst, S. et al. Chemical dispersants can suppress the activity of natural oil-degrading microorganisms. *PNAS* **112**, 14900–14905 (2015).
76. Uritskiy, G. V., DiRuggiero, J. & Taylor, J. MetaWRAP—a flexible pipeline for genome-resolved metagenomic data analysis. *Microbiome* **6**, 158 (2018).
77. Nurk, S., Meleshko, D., Korobeynikov, A. & Pevzner, P. A. metaSPAdes: a new versatile metagenomic assembler. *Genome Res* **27**, 824–834 (2017).
78. Langmead, B. & Salzberg, S. L. Fast gapped-read alignment with Bowtie 2. *Nat. Methods* **9**, 357–359 (2012).
79. Katoh, K. & Standley, D. M. MAFFT: Iterative Refinement and Additional Methods. in *Multiple Sequence Alignment Methods* (ed. Russell, D. J.) 131–146 (Humana Press, Totowa, NJ, 2014) https://doi.org/10.1007/978-1-62703-646-7_8.
80. Laczny, C. C. et al. VizBin - an application for reference-independent visualization and human-augmented binning of metagenomic data. *Microbiome* **3**, 1 (2015).
81. Chaumeil, P.-A., Mussig, A. J., Hugenholtz, P. & Parks, D. H. G. T. D. B.-Tk: a toolkit to classify genomes with the Genome Taxonomy Database. *Bioinformatics* **36**, 1925–1927 (2020).
82. Zhou, Z. et al. METABOLIC: high-throughput profiling of microbial genomes for functional traits, metabolism, biogeochemistry, and community-scale functional networks. *Microbiome* 1–22 (2022).

83. Shaffer, M. et al. DRAM for distilling microbial metabolism to automate the curation of microbiome function. *Nucleic Acids Res.* **48**, 8883–8900 (2020).
84. Yu, N. Y. et al. PSORTb 3.0: improved protein subcellular localization prediction with refined localization subcategories and predictive capabilities for all prokaryotes. *Bioinformatics* **26**, 1608–1615 (2010).

Acknowledgements

We thank the captain and crew of R/V Atlantis, the HOV Alvin team, and the shipboard scientific party for their help securing and processing samples during expedition AT42-05. We thank the Schmidt Ocean Institute for providing time at sea on R/V Falkor. We thank the captain and crew of R/V Falkor, the ROV SuBastian team, and the scientific crew during expedition FK190211 for assistance with sample collection and processing. This work was supported by the National Science Foundation's Biological Oceanography program through awards to S.B. Joye (OCE-1357360 and OCE-2049439), A.P. Teske (OCE-1357238), and K. Anantharaman (OCE- 2049478). The Schmidt Ocean Institute provided time at sea in the Gulf of California on board the R/V Falkor. This study was also supported in part by resources and technical expertise from the Georgia Advanced Computing Resource Center, a partnership between the University of Georgia's Office of the Vice President for Research and the Office of the Vice President for Information Technology, and by support provided by the University of Georgia's Office of the Provost and the Office of the Vice President for Research.

Author contributions

A.M., G.C.Z., H.C., and S.B.J. synthesized the initial ideas and sampling plan. A.M., H.C., Z.M., and G.C.Z. collected samples and conducted rate measurements. Z.M. assisted with processing of rate samples under A.M.'s supervision. A.M., H.C., K.H., and C.H. performed chemical analyses. Z.Z., M.V.L., and K.A. performed metagenomic analyses. M.C.M.M. and C.A.M.G. analyzed multibeam sonar data and provided maps and bathymetry data. The research expeditions were led by A.T. (AT42-05) and S.B.J. (FK190211). A.M. and S.B.J. prepared the manuscript, and all authors contributed critical comments and editorial feedback.

Competing interests

The authors declare no competing interests.

Additional information

Supplementary information The online version contains supplementary material available at <https://doi.org/10.1038/s41467-025-59793-0>.

Correspondence and requests for materials should be addressed to Samantha B. Joye.

Peer review information *Nature Communications* thanks Kai Tang and the other, anonymous, reviewer(s) for their contribution to the peer review of this work. A peer review file is available.

Reprints and permissions information is available at <http://www.nature.com/reprints>

Publisher's note Springer Nature remains neutral with regard to jurisdictional claims in published maps and institutional affiliations.

Open Access This article is licensed under a Creative Commons Attribution-NonCommercial-NoDerivatives 4.0 International License, which permits any non-commercial use, sharing, distribution and reproduction in any medium or format, as long as you give appropriate credit to the original author(s) and the source, provide a link to the Creative Commons licence, and indicate if you modified the licensed material. You do not have permission under this licence to share adapted material derived from this article or parts of it. The images or other third party material in this article are included in the article's Creative Commons licence, unless indicated otherwise in a credit line to the material. If material is not included in the article's Creative Commons licence and your intended use is not permitted by statutory regulation or exceeds the permitted use, you will need to obtain permission directly from the copyright holder. To view a copy of this licence, visit <http://creativecommons.org/licenses/by-nc-nd/4.0/>.

© The Author(s) 2025